Thermographic Image Processing Toolbox for Pulsed and Transient Thermography

by

Jared Eric Kretzmann

South Africa

March 2016

Foreword

The Thermographic Image Processing toolbox contains implementations of discussed techniques in literature for thermography. The toolbox was a byproduct of my master's thesis in the inspection of fiber reinforced composites using transient thermography. The application is however applicable to pulsed thermography and other materials. When a processing technique is selected the user will be provided an option to choose between 'decay' (pulsed) and 'heating' (transient) - other additional information may also be prompted. The image processing methods provided in this package include:

- Contrast methods (absolute, running, standard, normalized contrast)
- Differential absolute contrast (DAC)
- Interpolated differential absolute contrast (IDAC)
- Skewness & kurtosis
- Matched filters
- Fourier transform
- Wavelet transform (using the Morlet wavelet)
- Principal component thermography (PCT)
- Thermal signal reconstruction (TSR) with derivatives
- Multiscale retinex enhancement
- Markov error contrast
- Thermal harmonic distortion
- Dynamic thermal topography
- Histogram equalization
- Other basic image processing methods

The thermographic signal processing methods are not limited to that provided, but should be a good starting point for thermographic research and for the comparison of the various algorithms.

All techniques in the toolbox can be implemented using a sample thermal sequence provided ('*Sample32x32*'). The thermal sequence is taken from a step heating response of a 5 mm thick black, opaque Plexiglas® plate. The sample contains three 15 mm wide square flat-bottom holes at depths 1, 2 and 3 mm deep from left to right. The techniques can also be applied to other thermal sequences sharing the same data structure.

1. Overview

A graphical user interface (GUI) was developed to aid in the application of processing methods to thermographic sequences. The GUI provides the variety of algorithms applicable for both transient and pulsed thermal sequences. The main GUI interface is shown in Figure 1.1. The various panels designated by the numbers in the figure will be discussed below.

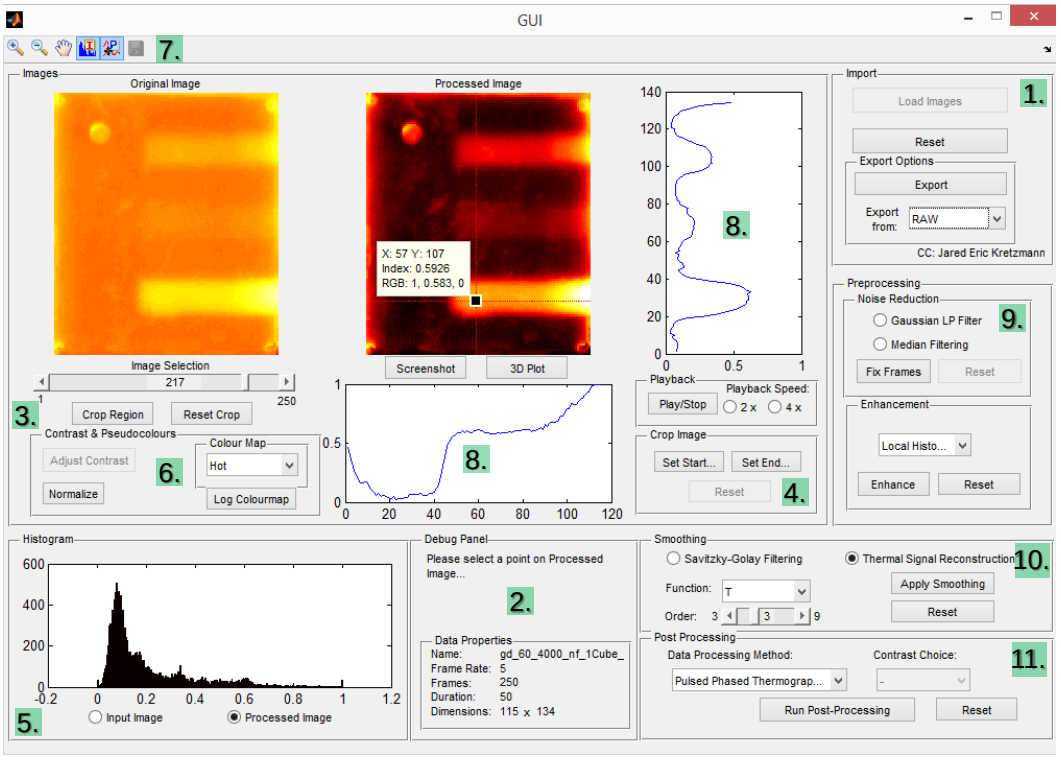

Figure 1.1: Graphical user interface (GUI) for thermography

The GUI was developed in Matlab® R2013b and requires little support from additional toolboxes or implementations of newer Matlab® versions.

1.1 Import and Export Sequence

The import panel provides import and export of raw or processed thermal sequences. The GUI supports the import of the following two data types: Matlab® binary (.mat) file and tagged image file format (.tiff). If the sequence consists of multiple files with in the selected directory, the files will be imported and reformatted into a single three-dimensional matrix in the order of date created.

A screenshot and a three-dimensional surface plot of the current process image can be produced by the appropriate buttons underneath the processed image.

1.2 Debug Panel

The debug panel provides assistance when using the GUI and displays when an algorithm is completed. Each algorithm will initiate its own wait-bar that will provide an estimated time of completion. The panel also displays the recording and image properties of the sequence.

1.3 Crop Image Region

The crop region button triggers a rectangular window that appears on the processed image allowing a user to crop the image dimensions for the entire sequence. This is beneficial for focusing in on a particular region of interest, which can subsequently increase the visual contrast of the cropped region. The reset crop button will reset the image dimensions to its previous state.

1.4 Crop Thermal Sequence

The crop image panel offers the ability to redefine the truncation window of the thermal sequence, or the number of frames. The image selection slider is used in conjunction with the appropriate push button to crop from the current image. The reset button will reset the image to its previous frame length.

1.5 Histogram Plot

The histogram panel provides both the original and processed image histogram options. The histogram allows inspection of the dynamic range where 0 and 1 respectively represent black and white intensities. Alternatively the histogram represents the distribution of the temperature range in the selected image.

1.6 Adjust Visualization

The contrast and pseudocolours panel enhances the visualization of the thermal sequence. Multiple colourmaps can be chosen along with logarithmic colourmap options. The adjust contrast tab allows manual clipping of high or low frequency bins to enhance the thermogram. The normalize button ensures that the dynamic range of an image has been fully utilized by the thermal data.

1.7 Image Tools

The toolbar panel provides common image tools, such as zoom and pan. Additional features include selection of an image pixel for displaying the temperature history (P) or the vertical and horizontal spatial profiles (I).

1.8 Display Axes

The two display axes plot either the temperature sequence (P) or the vertical and horizontal spatial profiles (I) of the selected pixel. The vertical and horizontal lines on the image designate the spatial profiles of the pixels of interest and are plotted on the corresponding display axes, seen in Figure 1.1.

1.9 Pre-processing

The pre-processing panel provides noise filters and spatial image enhancement algorithms, such as histogram equalization. The selected method is iterated over the entire sequence.

1.10 Signal Smoothing

The signal smoothing panel is an important tool for thermographic signals contaminated with noise. This can be used as another pre-processing method to reduce temporal noise. Both the smoothing methods provide first and second derivatives that can be selected by the drop-down box. The order slider provides the fitting polynomial order.

1.11 Post-processing

The post-processing panel provides a drop-down menu of the processing methods discussed in the next chapter. Particularly when the thermal contrast

processing method is selected the contrast choice drop-down box is enabled and provides a further selection of contrast options, such as absolute contrast and interpolated differential absolute contrast.

Note

The selected processing technique may save other relative thermal sequences in the current directory of the GUI. These sequences provide the alternative output not requested by the user. The saved sequence can be viewed by loading the .mat file into the GUI. For example when using the Fourier transform, the user may have selected the phase images, which would be displayed in the GUI while the amplitude images will be saved in current directory. This mitigates the need to run the processing method again for the alternative output option.

2. Image Toolbox Functions

The thermal contrast between defective and non-defective regions is normally weak and degraded by uneven distribution of heat, various noise sources, environmental reflections and optical variability in the target surface. Optical variability includes variations in local emissivity, surface cleanliness and non-planar geometries. Consequently the thermal contrast is typically poorer for flaws that represent real delaminations or voids. Therefore through the application of processing algorithms developed for thermographic inspection, the subtle anomalies can be enhanced to provide an optimal signal for qualitative and quantitative investigations.

2.1 Organization of the Thermal Sequence

The measured thermal signal should consist of a sequence of frames having a spatial resolution of $N_x \times N_y$ pixels. In order to suitably handle the thermal sequence the individual frames can be concatenated as a three-dimensional $N_x \times N_y \times N_t$ matrix where N_t defines the total number of frames in the sequence, shown in Figure 2.1. The number of frames is the product of total recording duration t_{acq} and sampling frequency f_s of the camera, i.e. $N_t = t_{acq} f_s$. The sampling frequency defines a time step Δt that describes the time resolution.

The signal can be processed as either a two-dimensional array (image) or on a pixel-wise basis of the temperature response over time. Two-dimensional processing methods are generally qualitative as they independently process each frame with no account of temporal information.

The thermal sequence should be formatted in a file structure as defined by Table 2.1. However the import process should handle the appropriate field names in the structure and will only request the recording frame rate.

2.2 Data Normalization

The temperature can be expressed as an excess surface temperature measurement that indicates a change in surface temperature after the heat has been applied to the target sample. To display the excess temperature as a grayscale

image, data normalization needs to be performed. Data normalization can be achieved by either two-dimensional or three-dimensional normalization methods defined as

$$I_{N_{2D/3D}} = (I - a)\frac{(d - c)}{(b - a)} + c, \tag{2.2.1}$$

where I is the original data set with a data range $[a, b]$ and I_N is the normalized data set for the desired range $[c, d]$. Data normalization does not change the quality of the raw signal as the thermal data is handled as a 16-bit array and equally displayed as a 16-bit indexed image.

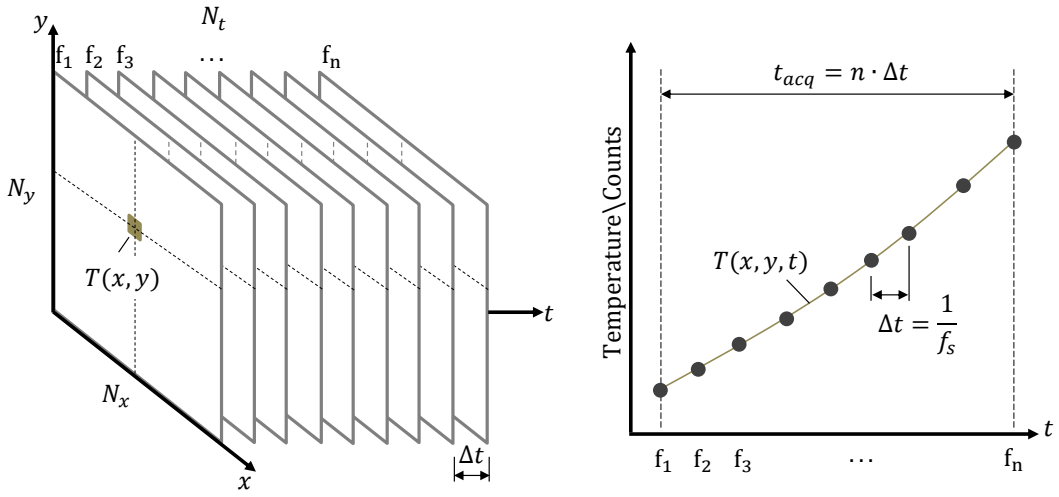

Figure 2.1: Thermal data cube and a pixel's temperature response over time

Table 2.1: Matlab file structure containing the three-dimensional thermal sequence and relevant metadata

Structure name	Description	Type
a	3D datacube	double; uint8,16; integer
b	Filename	string
c	Frame-rate f_s	value described in Hertz
d	Number of frames	integer, $\mathbb{Z}$
e	Total acquisition time t_{acq}	real number, $\mathbb{R}$
f	Image width (pixel)	integer, $\mathbb{Z}$
g	Image height (pixel)	integer, $\mathbb{Z}$

2.3 Spatial Enhancement Methods

Spatial enhancement methods originate from classical image processing methods and are commonly accepted as typical image enhancement methods found in most image processing handbooks. These methods are performed as a post-processing procedure to enhance the quality of the image.

2.3.1 Spatial Noise Reduction

Thermograms are prone to ambient and inherent camera noise. There are many ways to de-speckle or de-noise an image using linear, non-linear or even statistical operators. Linear filters are less preferred as they generally blur detail in the images. Two non-linear noise filters, Gaussian low-pass and adaptive median filter, are in the present work for reducing spatial noise.

2.3.2 Histogram Equalization

Histogram equalization (HE) is a common image processing technique of adjusting image contrast by redistributing the intensities of the image's histogram. HE allows the most frequent intensities to be redistributed to other intensity levels enabling lower frequency intensities such as the defect intensities to gain increased contrast. Modified HE methods have built on the classical HE method to reduce oversaturation and maintain finer detail in the image. The definitions for modified HE methods can be found elsewhere (Abdullah-Al-Wadud et al., 2007; Štruc et al., 2009; Park et al., 2008; Sheet et al., 2010).

2.3.3 Multiscale Retinex

The multiscale retinex (MSR) algorithm is a photometric normalization technique proposed by Jobson et al. (1997) from the field of facial recognition and has been used in X-ray photography (Rahman et al., 2001). The MSR performed well on enhancing detail and removal of uneven-heating compared to other photometric normalization techniques. This method is seen to resemble how our eyes (retina) perceive variations in grayscale intensities.

Photometric normalization is a technique of separating the image into two components, namely an illumination image containing low spatial frequencies and reflectance image containing high spatial frequencies. The high spatial frequencies represents edges and higher level of detail and this image will present an enhanced image with higher level of detail

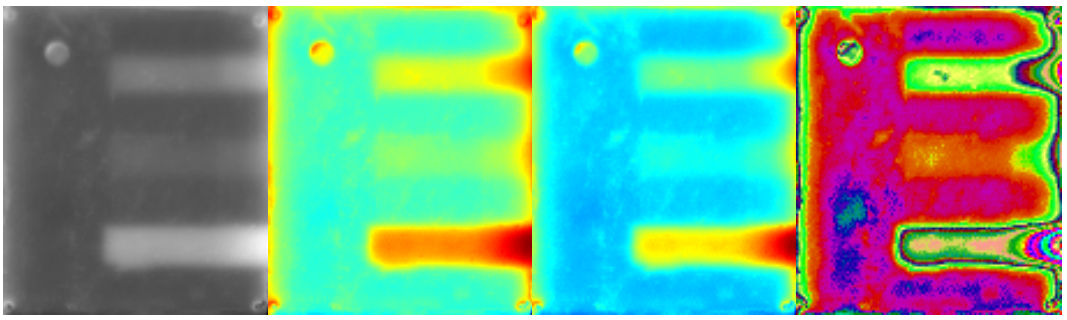

(a) Grayscale (b) Jet (c) Logarithmic jet (d) Complementary

Figure 2.2: The benefits of colourmaps on thermograms

2.3.4 Pseudo-Colour Images

Pseudo-colours are used to instantly highlight any irregularities in the grayscale images. This is a result of colour receptors (cones) of a human eye having a higher spatial acuity compared to that of rods, which are responsible for low light vision. Pseudocolours systematically map each grayscale intensity to a colour according to a colour table.

Figure 2.2 shows a variety of common colour maps. A new colourmap is proposed using complementary colours as seen in Figure 2.2d. When complementary colours are put together they create the strongest contrast. Therefore any slight change in intensity will be more pronounced with this map. The choice of colourmap depends on the image itself. Logarithmic colourmaps are more appropriate than linear colourmaps for visualizing thermograms (Klein et al., 2008) as seen in Figure 2.2c.

2.4 Thermal Contrast Enhancement

The simplest form of enhancing detail in a thermogram is through thermal contrast enhancement. Each of these methods require the selection of a sound area S_a which can be one pixel or the average of selected sound areas. The differential absolute contrast and modified differential absolute contrast methods do not require the selection of a sound area S_a but rather an image frame before defects begin to appear.

2.4.1 Absolute Contrast

Absolute contrast is the classical and most basic contrast definition describing the excess temperature over a defect-free region:

$$C_{abs}(t) = T(t) - T_{S_a}(t) \tag{2.4.1}$$

where $T(t)$ is the temperature for any pixel and $T_{S_a}(t)$ is the temperature for chosen sound area at time t.

2.4.2 Standard Contrast

Standard contrast was developed to suppress the impact of reflections produced by the surrounding environment through subtraction of an image's pixels at time t_0 before heating (Maldague, 2001):

$$C_{std}(t) = \frac{T(t) - T(t_0)}{T_{S_a}(t) - T_{S_a}(t_0)}. \tag{2.4.2}$$

2.4.3 Normalized Contrast

Variations in surface emissivity shift the amplitude of the thermal time history of each pixel making the subtraction of a sound zone less effective. Normalized contrast operates on normalizing each pixel with respect to the time of maximum temperature, t_{max} or the end of the sequence, t_{end}. The method is intended to minimize variability in optical effects that include emissivity, non-uniform heating and absorptivity lengths (Balageas et al., 1991, Balageas et al., 2012). The normalized contrast is defined as

$$C_{norm}(t) = \frac{T(t)}{T(t_{max})} - \frac{T_{S_a}(t)}{T_{S_a}(t_{max})}. \tag{2.4.3}$$

2.4.4 Running contrast

The running contrast reduces the effects of differences in surface emissivity as it normalizes each pixel with the temperature of the chosen sound area S_a at a time t. The running contrast is defined as (Maldague, 2001)

$$C_{run}(t) = \frac{T(t) - T_{S_a}(t)}{T_{S_a}(t)} = \frac{C_{abs}(t)}{T_{S_a}(t)} \tag{2.4.4}$$

2.4.5 Differential Absolute Contrast (DAC)

The differential absolute contrast (DAC) removes the need for the manual selection of a sound area S_a. The technique was originally based on the Dirac delta function for pulsed thermography (González et al., 2004a), which has now been extended to step thermography.

The differential absolute contrast is a form of extrapolated contrast based on the extrapolation of temperature at early times through the one-dimensional semi-infinite model at the surface $z = 0$ of the specimen. The contrast is formulated on the assumption that a sound zone is expected to follow the semi-infinite model for early times t:

$$\Delta T_{\infty}(t) \approx \Delta T_{S_a}(t), \tag{2.4.5}$$

where the half-space semi-infinite model for step heating is

$$\Delta T_{\infty}(t) = \frac{2Q}{e}\frac{\sqrt{t}}{\sqrt{\pi}}. \tag{2.4.6}$$

At a time t' just after heating and before an actual defect becomes visible the measured temperature at the surface of the specimen is assumed to behave as an ideal sound area S_a, i.e. $\Delta T_{meas}(t') = \Delta T_{S_a}(t')$. At this time the surface has not been affected by the existence of a internal defect and therefore the local temperature of a defective area is exactly the same for a sound zone. A practical assumption is made that follows Equation 2.4.5 where the measured temperature ΔT_{meas} at t' is equal to the half-space semi-infinite model at t' (Klein et al., 2008). This can be defined for a step pulse at time t' as

$$\Delta T_{\infty}(t') = \frac{2Q}{e}\frac{\sqrt{t'}}{\sqrt{\pi}} = \Delta T_{meas}(t'), \tag{2.4.7}$$

where $\Delta T_{meas}(t')$ and t' are known measurements from the thermal data. Now Equation 2.4.7 is expressed for Q/e as

$$\frac{Q}{e} = \Delta T_{meas}(t')\ \frac{1}{2\sqrt{\pi t'}}. \tag{2.4.8}$$

Substituting Q/e into Equations 2.4.5 and 2.4.6, the extrapolated temperature of a sound area is defined as

$$\Delta T_{S_a}(t) \approx \sqrt{\frac{t}{t'}}\ \Delta T_{meas}(t'). \tag{2.4.9}$$

Using the absolute contrast definition (Eq. 2.4.1), the extrapolated thermal contrast is defined using the difference of the measure temperature $\Delta T_{meas}(t)$ and extrapolated temperature $\Delta T_{S_a}(t)$:

$$\Delta T_{DAC}(t) = \Delta T_{meas}(t) - \sqrt{\frac{t}{t'}}\ \Delta T_{meas}(t'). \tag{2.4.10}$$

The DAC method is only valid for early times as at later times the thermal response of both the sound and defective areas deviates from the semi-infinite model where $\Delta T_{\infty}(t) \neq \Delta T_{S_a}(t)$.

2.4.6 Interpolated Differential Absolute Contrast (IDAC)

The interpolated differential absolute contrast (IDAC) explicitly introduces the sample's thickness by means of solving the one-dimensional heat problem in the Laplace space using thermal quadrupoles, before computing the

inverse Laplace transform (Benetiz et al., 2006). The IDAC is a modification to the DAC method described above, which performs temperature extrapolation of a one-dimensional model. However the extrapolation follows the one-dimensional model of finite slab thickness. This algorithm requires knowledge of the material's diffusivity and thickness.

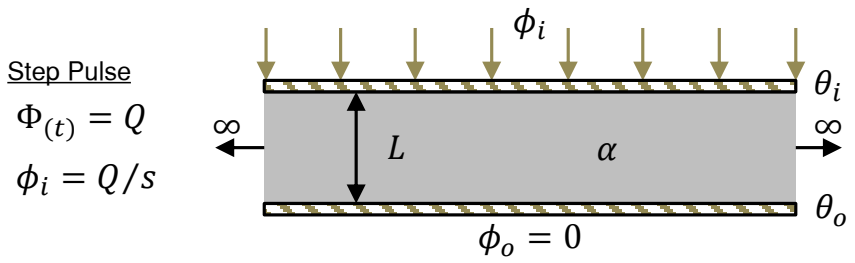

Figure 2.3: Insulated slab model in Laplace space

Figure 2.3 illustrates a thermal model of an insulated slab in Laplace space with boundary and initial conditions. To describe the boundary and initial conditions let the Laplace transform of the surface temperature be defined as $\mathcal{L}\left(\Delta T_{slab}(t)\right) = \theta_i(s)$ and let the heat flux density function be defined as $\mathcal{L}\left(\Phi(t)\right) = \phi_i(s)$ for a Laplace variable s. The rear-wall Laplace temperature, and heat flux density can be respectively defined as outputs $\theta_o(s)$ and $\phi_o(s)$. The problem can be solved through the thermal quadrupole equation knowing only the values at $z = 0$ and $z = L$:

$$\begin{pmatrix} \theta_i \\ \phi_i \end{pmatrix} = M \cdot \begin{pmatrix} \theta_o \\ \phi_o \end{pmatrix} \qquad \text{with} \qquad M = \begin{pmatrix} A & B \\ C & D \end{pmatrix}, \tag{2.4.11}$$

where the quadrupole matrix M for a solid slab is

$$\begin{aligned} A = D = \cosh(\kappa L), \qquad & B = \sinh(\alpha L)/(\kappa k), \\ C = \alpha\kappa \ \sinh(\alpha L), \qquad & \kappa = \sqrt{s/\alpha}. \end{aligned} \tag{2.4.12}$$

The Laplace quadrupole in Equation 2.4.11 can be alternatively expressed as:

$$\theta_i = A\theta_o + B\phi_o \tag{2.4.13}$$

$$\phi_i = C\theta_o + D\phi_o \tag{2.4.14}$$

The Laplace transform of surface heat flux density for step heating are $\phi_i = \mathcal{L}(\Phi_{(t)}) = Q/s$ (Maillet et al., 2000). Taking into account $\phi_o = 0$ since the plates rear-wall is assumed adiabatic and knowing ϕ_i, the Laplace surface temperature can be expressed as

$$\theta_i = \frac{QA}{sC} = \frac{Q}{e}\,\frac{\coth\sqrt{sL^2/\alpha}}{s\sqrt{s}} = \frac{Q}{e}\,\theta_i' \tag{2.4.15}$$

Solving in a similar manner to the DAC method, the change in temperature of the sound zone can be approximated by the inverse Laplace of the the surface temperature:

$$\Delta T_{slab}(t) = \mathcal{L}^{-1}(\theta_i)|_t = \frac{Q}{e}\mathcal{L}^{-1}(\theta_i')|_t \approx \Delta T_{S_a}(t) \tag{2.4.16}$$

where the inverse Laplace requires a numerical approximation that can be performed by either Talbot's method (Abate & Whitt, 2006) or Gaver-Stehfest algorithm (Stehfest, 1970). Because $\Delta T_{meas}(t')$ can be expressed as

$$\Delta T_{meas}(t') = \Delta T_{slab}(t') = \frac{Q}{e}\ \mathcal{L}^{-1}(\theta_i')|_{t'}, \tag{2.4.17}$$

in this extrapolated contrast method, a Q/e function can be rewritten once again and introduced into Equation 2.4.16:

$$\Delta T_{S_a}(t) \approx \frac{\mathcal{L}^{-1}(\theta_i')|_t}{\mathcal{L}^{-1}(\theta_i')|_{t'}}\Delta T_{meas}(t') \tag{2.4.18}$$

Therefore the modified DAC is calculated as the difference between the measured and extrapolated sound region:

$$\Delta T_{IDAC} = \Delta T_{meas}(t) - \frac{\mathcal{L}^{-1}(\theta_i')|_t}{\mathcal{L}^{-1}(\theta_i')|_{t'}}\Delta T_{meas}(t') \tag{2.4.19}$$

The IDAC for pulsed thermography is formulated in the same manner but this time $\phi_i = \mathcal{L}(\Phi_{(t)}) = Q$ for a Dirac delta function in the Laplace space.

2.4.7 Normalized DAC Methods

Both DAC methods introduced so far are insensitive to surface non-uniformities and produce relatively flat sound regions. However regions other than sound zones are still affected by surface emissivity and local heating effects producing changes in temperature amplitudes. To account for this problem, the DAC methods can be normalized as follows (Klein et al., 2008)

$$\Delta T_{normalizedDAC}(t) = \frac{\Delta T_{measured}(t)}{\Delta T_{measured}(t')} - \frac{\mathcal{L}^{-1}(\theta_i')|_t}{\mathcal{L}^{-1}(\theta_i')|_{t'}}, \tag{2.4.20}$$

which allows better quantitative estimations even though the images may not be visually appealing.

2.4.8 Markov Error Contrast

The Markov error contrast is defined as the error between the actual and an estimated temperature T_{est} for each individual pixel's time sequence (Larson, 2011)

$$E(t) = T(t) - T_{est}(t). \tag{2.4.21}$$

The Markov error contrast is based on a Markov chain treating each temperature in the pixel's time sequence as independent. In order to evaluate the error at time t an estimated temperature is required at the same time. Thus the estimated temperature can be calculated as a function of the previous temperature in time and repeated until each temperature has synthetically been reconstructed. Using a simplified one-dimensional response for step heating (recall (Eq. 2.4.10) the estimated temperature can be evaluated. In this case the Markov error will represent and amplify any deviation from an ideal sound area S_a response. The estimated temperature can therefore be calculated by using a modified version of Equation 2.4.10:

$$T_{est}(t) = T(t-1) \cdot \sqrt{\frac{t-1}{t}}\ , \tag{2.4.22}$$

where $T(t-1)$ is the previous temperature at a current time t in thermal sequence.

2.5 Signal Transforms

The signal transforms are based on the fact that it is possible to reconstruct any continuous function in another domain space. Two methods have been proposed to enhance overall defect detectability and provide inversion techniques for depth. These methods are known as the Fourier transform (FT) and wavelet transform (WT). Both transforms reconstruct the pixel's temperature signal in the frequency space where amplitude and phase images can be retrieved. Phase images have shown to be less affected by surface emissivity, surface features and non-uniform contrasts.

2.5.1 Fourier transform

The one-dimensional discrete Fourier transform is applied to the temperature history of each pixel $T(t)$ as (Ibarra-Castanedo, 2005)

$$F_k = \Delta t \sum_{n=0}^{N-1} T(n\Delta t)\, \exp^{-\jmath 2\pi nk/N}, \qquad k \in \mathbb{Z}, \tag{2.5.1}$$

where $j^2 = -1$, $n = (0, 1, 2, \cdots, N-1)$ defines the next sampling time for N sample points separated by a sampling interval Δt and k designates the frequency increment ($k = 0, 1, 2, \cdots, N$). The Fourier transform is defined to cover infinite frequencies $k \to \infty$, but considering that there is a finite number of time samples defined by the signal of length N_t, the number of frequencies needed to adequately represent the signal is $N \geqslant N_t$. Because the signal is non-periodic, the signal is typically zero-padded and in this case $N \approx 2N_t$ which provides enough sampling frequencies.

The complex exponential term of the Fourier coefficients produces a real and complex term, $F_k = \mathrm{Re}_k + j\mathrm{Im}_k$, which can be separated to produce discrete amplitude A and phase ϕ data:

$$A_k = \sqrt{\mathrm{Re}_k^2 + \mathrm{Im}_k^2}, \tag{2.5.2}$$

$$\phi_k = \mathrm{atan}\left(\frac{\mathrm{Im}_k}{\mathrm{Re}_k}\right). \tag{2.5.3}$$

The resulting one-dimensional amplitude and phase data can be separately reshaped to produce a series of amplitude and phase images.

The amplitude and phase signal produces frequencies ranging from f_1 to f_N in Hz as illustrated in Figure 2.4. The number of discrete frequency samples correspond to the number of discrete time samples N. However, only half of the frequencies needs to be considered as the amplitude and phase images are symmetrical about frequency $f_{N/2}$. The available frequency components do not represent 'real' frequencies but can be calculated directly from the time domain as (Maldague, 2001)

$$f = \frac{n}{N\Delta t} = \frac{n}{N} f_s, \tag{2.5.4}$$

where the minimum available frequency is defined as $f_{min} = f_s/N$ and the maximum available frequency is half the sampling frequency ($f_{max} = f_s/2$), also known as the Nyquist or critical frequency f_c. The available frequencies follow the Nyquist-Shannon sampling theorem where a function can be completely recovered from the sampled data without aliasing provided that the sample frequency f_s is at least twice the maximum available frequency or $f_c \geq 1/2\ f_s$ (Shannon, 1949). This feature of the Fourier transform can be used to evaluate the optimal sampling rate for transient thermography by comparing the maximum available frequency of different camera sampling frequencies.

Generally the Fourier transform can be performed with little attention to the data, however under-sampling and poorly truncated data has an affect on the performance of the transform in defect estimation methods (Ibarra-Castanedo, 2005). Poorly defining the data truncation window, i.e. the beginning and end of the thermal sequence after all defects have emerged, affects the overall frequency resolution. An increase in error was observed for depth estimation for a smaller truncation window in pulsed thermography.

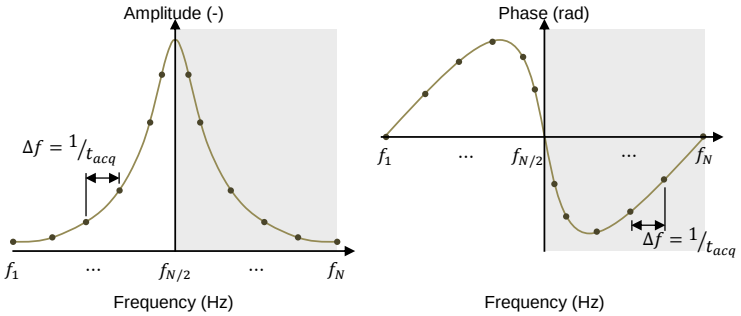

Figure 2.4: Amplitude (left) and phase (right) profiles produced by the Fourier Transform on a pixel's temperature response (adapted from Ibarra-Castanedo, 2005)

Zero padding does not improve the frequency resolution but improves the ability to distinguish between adjacent frequencies. The poorly truncated data suffers from leakage in the frequency spectrum where frequency energy is distributed over a wider frequency range and thus reducing the maximum phase contrast. The FFT computation assumes the signal is periodic. In the case of transient thermography, the signal satisfies the periodic requirement as the signal starts at zero at the beginning of the time window and then rises to some maximum and decays again to zero before the end of the time window. This can be seen as a quarter wave of a periodic signal and presents no sharp changes. However the square pulse temperature response produces a sharp change between the the heating and cooling phases which may reduce the effectiveness of this method.

2.5.2 Wavelet Transform

The wavelet transform is the extension of the Fourier transform with the added benefit of preserving time information, since defect depth is a function of the square root of time. Instead of decomposing the signal by a continuous sinusoidal function, as in Fourier transform, the signal is decomposed through window functions containing a periodic waveform of limited duration, known as a wavelet. The basic wavelet transform can be seen as the convolution of the signal $f(t)$ and daughter wavelet $\psi_{S,Tr}(t)$ defined for a translation factor Tr and a scale factor S:

$$W_f(S,Tr) = \int_{-\infty}^{\infty} f(t)\ \psi^*_{S,Tr}(t)\ \mathrm{dt}, \qquad S, Tr \in \mathbb{R}_{>0} \tag{2.5.5}$$

where * is the complex conjugate. The daughter wavelet $\psi_{S,Tr}(t)$ is expressed as a scaled and translated replica of a single base wavelet called the mother wavelet $\psi_m(t)$:

$$\psi_{S,Tr}(t) = \frac{1}{\sqrt{|S|}}\ \psi_m\ \left(\frac{t-Tr}{S}\right) \tag{2.5.6}$$

where the scaling factor S controls the width of the wavelet and the translation factor Tr controls the position of the wavelet along the analysed signal. The wavelet transform permits the use of many different mother wavelets $\psi_m(t)$. The choice of the wavelet should be chosen to best represent the signal or possess a distinct characteristic of the signal. The choice of the wavelet for thermographic analysis is desired to share the characteristic qualities of the Fourier transform and, hence, the complex Morlet wavelet is chosen as the mother wavelet (Zauner et al., 2010; Galmiche & Maldague, 2000; Maldague et al., 2002). The Morlet mother wavelet is defined as

$$\psi(t) = \exp^{(-\jmath\omega_0 t)} \cdot \exp^{\left(-\frac{t^2}{2}\right)}, \tag{2.5.7}$$

where $\omega_0 = 2\pi f_0$ describes the center frequency (f_0) that defines the initial scale of Morlet wavelet and number of significant oscillations within the window. Figure 2.5 shows the real and imaginary parts of two daughter wavelets of the complex Morlet wavelet at different scales. The complex Morlet wavelet can be seen to exhibit a symmetric Gaussian envelope of a sinusoidal function with a center frequency illustrated by the dashed sinusoidal function. By altering the scale of the wavelet the center frequency is changed which is the reason the wavelet can decompose the signal into various frequency components. Consequently, amplitude and phase data become available.

More importantly the Morlet wavelet has an optimal joint time-frequency concentration since it has an exponential decay in both the time and frequency domains. This means that there is an equal trade-off between frequency and time support using this wavelet and this support is not observed in many other mother wavelets.

The output of the wavelet transform produces a tiling in the translation-scale plane that corresponds to a time-frequency plane as seen in Figure 2.6. The entire set of tiles describes the decomposition of a one-dimensional data signal and can be combined to reconstruct the original signal. The relation between wavelet scale S and a pseudo-frequency can be established as (Zauner et al., 2010)

$$f_{pseudo} = \frac{f_0}{S \cdot \Delta t}, \tag{2.5.8}$$

where f_{pseudo} is in Hz corresponding to scale, center frequency and sampling period. The widths and heights of the tiles respectively define the time and frequency resolution (or support) of a wavelet at a given scale S. The width of the windowing function limits both the time and frequency resolution of the tile according to Heisenberg uncertainty principle (Zauner et al., 2010):

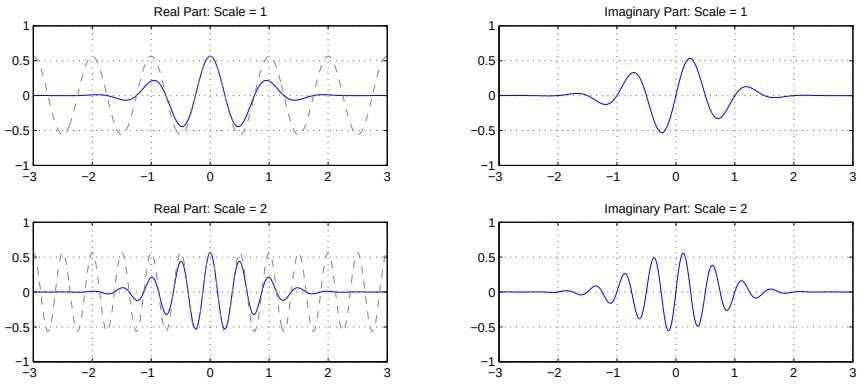

Figure 2.5: Real and imaginary parts of a Morlet wavelet for a change in scale S affecting the center frequency (dashed line)

$$\Delta t \cdot \Delta\omega \geq \frac{1}{2}, \tag{2.5.9}$$

which describes the joint time-frequency resolution. This principle can be observed as theoretical boxes in Figure 2.6. When the scale S increases in the direction of the arrow in Figure 2.6, the time support is increased, i.e. less repeating tiles, but with a reduction in the frequency resolution. As a result lower frequency components of the thermal response are observed. The opposite is observed for a decrease in scale where the frequency resolution increases and higher frequency components have less time support. This is another interesting feature of the wavelet transform that the high frequency components can be separated as they are assumed to represent noise terms and the signal can be reconstructed without noise. The initial choice ω_0 can be observed to have a similar effect as the scaling factor on frequency and time precision, where a larger ω_0 produces a smaller frequency resolution $\Delta\omega$ and greater uncertainties over translation factor and thus over defect depth. Galmiche & Maldague (2000) selected a center frequency of $\omega_0 = 2$ to reduce uncertainties in depth estimation.

The wavelet transform can be implemented using the fast Fourier transform (FFT) which conveniently handles the time-shift parameter, Tr, and the convolution can efficiently take place in the frequency domain - the convolution theorem states that convolution in time domain corresponds to multiplication in frequency domain. The simple multiplication of the signal and daughter wavelet can be computed and repeated for multiple scales:

$$W_f = \text{IFFT}[\text{FTT}(f(t)) \cdot \text{FFT}(\psi_S(t))] = \text{Re}_S + \jmath\text{Im}_S \tag{2.5.10}$$

where the translation factor Tr is controlled by the FFT algorithm and reiterated for scales $S > 0$. The inverse fast Fourier transform, IFFT, is performed

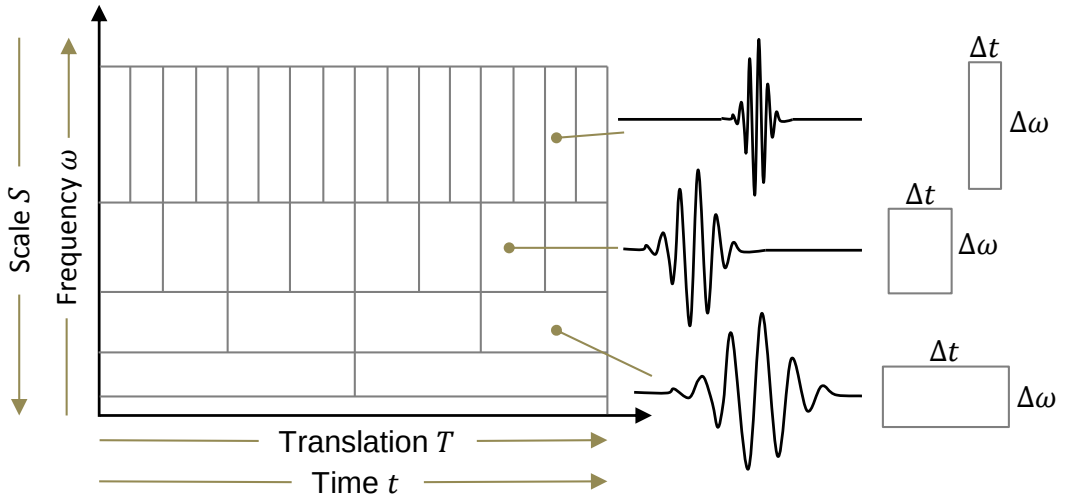

Figure 2.6: Scale-translation plane of a one-dimensional signal depicting the Heisenberg uncertainty relationship between frequency resolution and time resolution

to produce the real and complex parts to extract the amplitude (Eq. 2.5.2) and phase data (Eq. 2.5.3) for each scale S.

The wavelet transform produces two-dimensional time-scale data from an one-dimensional temperature signal. Even though the fast Fourier transform is relatively efficient, the wavelet transform is computational expensive and requires a considerable number of computations and storage. To reduce the dimensionality and computations, Galmiche & Maldague (2000) proposed using the characteristic time relationship of emerging defect at depth z for determining the optimal scale for each time interval. Using the approximated characteristic time

$$t = \frac{z^2}{\alpha}, \tag{2.5.11}$$

a time as a function of frequency can be determined by equating the thermal diffusion length $\mu = \sqrt{\frac{2\alpha}{\omega}}$, which is the maximum penetration depth at each frequency, to depth z. This leads to the following relationship:

$$t = \frac{2}{\omega}. \tag{2.5.12}$$

The scale factor can be defined as the relationship between the center frequency and scale frequency as $S = \omega_0/\omega$. Knowing that the translation factor corresponds to time, the following relation allows the calculation of one scale factor for each translation time

$$S = \frac{\omega_0}{2} Tr. \tag{2.5.13}$$

The values of S and T are now limited by the actual acquisition time and hence the wavelet transform is (Galmiche & Maldague, 2000):

$$W_f(S,Tr) = \int_{-\infty}^{\infty} f(t) \frac{1}{\sqrt{0.5 \cdot \omega_0 \cdot Tr}} \psi(\frac{\frac{t}{Tr} - 1}{0.5 \cdot \omega_0}) \text{ dt} \tag{2.5.14}$$

2.6 Statistical Techniques

Descriptive statistical methods have been applied to express variability of a data set as images. The methods discussed here are automatic processing methods that require no user input. The statistical methods have been used as an image enhancement method that describes the entire thermal sequence as a single image.

2.6.1 Skewness

Skewness is the third standardized central moment that measures the asymmetry of the probability distribution in a univariate data set. Skewness is defined as (Madruga et al., 2008)

$$\text{skewness}(x_{ij}) = \frac{\sum_{k=1}^{N}(x_k - \mu)^3}{\sigma^3(N_T - 1)}, \tag{2.6.1}$$

where μ and σ are the mean and standard deviation of the temperature response of pixel x_{ij}. The subscripts i,j indicate the process is repeated for all pixel temperature sequences.

2.6.2 Kurtosis

Kurtosis is the fourth standardized moment that measures flatness of the central mean of the probability distribution in a univariate data set. Data sets with high kurtosis tend to have a distinct peak near the mean and low kurtosis have a flat top. Kurtosis is the next moment after skewness defined as (Madruga et al., 2009; Usamentiaga et al., 2012)

$$\text{kurtosis}(x_{ij}) = \frac{\sum_{k=1}^{N}(x_k - \mu)^4}{\sigma^4(N - 1)}. \tag{2.6.2}$$

2.6.3 Matched Filters

There are a few types of matched filtering algorithms but they all are based on the following model (Foy, 2009; Larson, 2011):

$$T_{meas} = \epsilon \, T_{refl} + T_{ideal} \ , \tag{2.6.3}$$

where T_{meas} is the measured temperature response that can be expressed by a temperature response caused by reflectance of defects, T_{refl}, and an ideal temperature response typical of a sound area, T_{ideal}. The strength of the reflected signal is indicated by ϵ. From Equation 2.6.3, the temperature sequences can be written in vector form:

$$\mathbf{x} = \epsilon\, \mathbf{s} + \mathbf{w} \ , \tag{2.6.4}$$

where $\mathbf{x} = T_{meas}$, $\mathbf{s} = T_{refl}$ and $\mathbf{w} = T_{ideal}$. Match filtering techniques require Equation 2.6.4 to be multiplied by a vector $\mathbf{q}$ that maximises the reflectance response and minimizes the sound area response. Hence, vector $\mathbf{q}$ can be determined by the objective function and the constraint

$$\max_{\mathbf{q}} ||\mathbf{q}^T\mathbf{s}|| \ \text{ subject to } \ \min_{\mathbf{q}} ||\mathbf{q}\mathbf{w}|| \ , \tag{2.6.5}$$

where the difference between the various matched filter detectors is defined by the method of determining the objective vector $\mathbf{q}$.

The match filters require the reflectance temperature sequence T_{refl} and ideal temperature sequence T_{ideal} to be known. One can obtain T_{ideal} by manually selecting a sound pixel but unfortunately T_{refl} is unknown. Therefore T_{refl} can be obtained by the following difference between the ideal and measured response assuming ϵ is one (Larson, 2011):

$$T_{refl} = T_{meas} - T_{ideal} \ . \tag{2.6.6}$$

The signal-to-noise ratio was noticed to increase for multiple selections of defective and sound pixels and taking the average respectively to represent T_{refl} and T_{ideal}.

2.6.3.1 Spectral Angle Map

The spectral angle map (SAM) is based on a simple match filter (SMF) where the T_{refl} sequence is used as $\mathbf{q}$. A resulting correlation image between the reflection and measured response is defined as

$$\text{SMF} = \mathbf{s}^{\mathrm{T}}\mathbf{x}_{ij} \ , \tag{2.6.7}$$

where again the subscript i,j indicate the process is repeated for all pixel temperature sequences.

The spectral angle map (SAM) defines the normalized vector magnitudes as

$$\text{SAM}(x_{ij}) = \frac{\mathbf{s}^{\mathrm{T}}\mathbf{x}_{ij}}{\sqrt{\mathbf{s}^{\mathrm{T}}\mathbf{s}}\sqrt{\mathbf{x}_{ij}^{\mathrm{T}}\mathbf{x}_{ij}}} \ . \tag{2.6.8}$$

The SAM image is a similar concept to correlation techniques and describes the cosine angle between the reflectance signal $\mathbf{s}$ and measured signal $\mathbf{x}$.

2.6.3.2 Adaptive Coherence Estimator (ACE)

The adaptive coherence estimator (ACE) is an extension of the clutter matched filter (CMF). The CMF includes the covariance matrix $\mathbf{C}$ of the data set, which incorporates the structural information of the target specimen. The filter is derived from the Likelihood Ratio Test which expresses the probability how many times more likely the data falls under one model than the other (Borokov, 1999). This effectively creates a unique threshold for each pixel. The CMF is defined as

$$\text{CMF} = \mathbf{s}^{\mathrm{T}}\ \mathbf{C}^{-1}\mathbf{x}_{ij}, \tag{2.6.9}$$

where $\mathbf{C}$ is the covariance matrix of the ideal response and is determined for the total number of pixels, $MN = M \times N$:

$$\mathbf{C} = \frac{1}{MN}\sum_{k=1}^{MN}\mathbf{w}_{ij}^{\mathrm{T}}\mathbf{w}_{ij}. \tag{2.6.10}$$

The ACE matched filter for normalized vector magnitudes is

$$\text{ACE}(x_{ij}) = \frac{\mathbf{s}^{\mathrm{T}}\ \mathbf{C}^{-1}\mathbf{x}_{ij}}{\sqrt{\mathbf{s}^{\mathrm{T}}\ \mathbf{C}^{-1}\mathbf{s}}\ \sqrt{\mathbf{x}_{ij}^{\mathrm{T}}\ \mathbf{C}^{-1}\mathbf{x}_{ij}}} \tag{2.6.11}$$

2.6.3.3 t-Statistic & F Statistic

The t-statistic and F statistic methods are common tools used in linear regression and their derivations can be found in literature (Foy, 2009). The definition for the t-statistic is

$$\text{t-stat} = \frac{\mathbf{s}^{\mathrm{T}}\mathbf{C}^{-1}\mathbf{x}_{ij}}{\sqrt{\mathbf{x}_{ij}^{\mathrm{T}}\mathbf{C}^{-1}\mathbf{x}_{ij} - \varrho^2(\mathbf{s}^{\mathrm{T}}\mathbf{C}^{-1}\mathbf{x}_{ij})^2}}\varrho\sqrt{d-1}\ , \tag{2.6.12}$$

and the F statistic is the square of the t-statistic:

$$\text{Fstat} = \frac{(\mathbf{s}^{\mathrm{T}}\mathbf{C}^{-1}\mathbf{x}_{ij})^2}{\mathbf{x}_{ij}^{\mathrm{T}}\mathbf{C}^{-1}\mathbf{x}_{ij} - \varrho^2(\mathbf{s}^{\mathrm{T}}\mathbf{C}^{-1}\mathbf{x}_{ij})^2}\varrho(d-1)\ , \tag{2.6.13}$$

where $\varrho = \frac{1}{\sqrt{\mathbf{s}^T\mathbf{C}^{-1}\mathbf{s}}}$.

2.7 Principal Component Thermography (PCT)

The Fourier transform is a convenient way of decomposing the thermal signals to the phase-frequency space through a set of sinusoidal basis functions, however transient signals are not periodic signals, particularly in the case of square

pulse heating. Sinusoidal functions indeed may not be the best choice for representing either transient heating signals. Principal component thermography (PCT) is based on an eigenvector transform which applies an orthogonal transformation to the thermal inspection data. PCT relies on singular value decomposition (SVD) which closely matches principal component analysis and are both used to reduce high-dimensional data into fewer dimensions while retaining relevant information. The only difference is that there is no need to calculate the covariance matrix which can lead to numerical rounding errors when evaluating the eigenvalues. Eigenvectors can be portrayed as axes along which a linear transformation acts by simple compression or stretching of data on orthogonal axes. Since eigenvalues are orthonormal they represent a complete description of the spatial and temporal variability in the entire thermal sequences as a smaller set of orthogonal statistical modes.

Assuming that the thermal data is a $M \times N$ data matrix $\mathbf{A}$ ($M > N$), then the SVD can be applied as follows (Rajic, 2002; Marinetti et al., 2004):

$$\mathbf{A} = \mathbf{URV}^{\mathrm{T}} \tag{2.7.1}$$

where $\mathbf{U}$ is a $M \times N$ matrix , $\mathbf{R}$ is a diagonal $N \times N$ matrix containing the absolute values of the eigenvalues (singular values) of $\mathbf{A}$ and $\mathbf{V}^{\mathrm{T}}$ is an $N \times N$ unitary matrix. In order to apply this to the thermal data-cube matrix, the total number of pixels are rearranged into a single vector to condense the information as a single matrix $\mathbf{A}$ having dimensions $(N_x \cdot N_y) \times N_T$ with time along the columns. Figure 2.7 shows the reorganised matrix $\mathbf{A}$ and the resulting orthogonal matrices produced by the SVD.

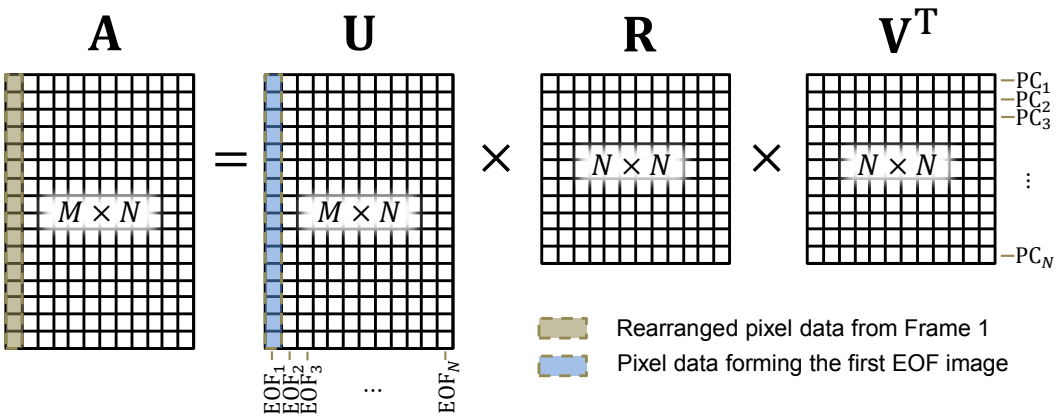

Figure 2.7: Reorganised matrix $\mathbf{A}$ of the thermal sequence and the resulting orthogonal sets using singular value decomposition depicting locations of EOFs and PCs

Each column vector of matrix $\mathbf{A}$ needs to be standardized to ensure uniform variance on a pixel-wise basis

$$\hat{\mathbf{A}}(m,n) = \frac{\mathbf{A}(m,n) - \mu_m}{\sigma_m}, \tag{2.7.2}$$

where

$$\mu_m = \frac{1}{N}\sum_{n=1}^{N}\mathbf{A}(m,n), \tag{2.7.3}$$

$$\sigma_m^2 = \frac{1}{N-1}\sum_{n=1}^{N}(\mathbf{A}(m,n) - \mu_n)^2. \tag{2.7.4}$$

Now the standardized matrix $\hat{\mathbf{A}}$ can be factorized using Equation 2.7.1. Orthogonal statistical modes are present in the columns of $\mathbf{U}$ known as the empirical orthogonal functions (EOFs) seen in Figure 2.7. The first few EOFs describe the largest variability in the thermal sequence and generally only a few EOFs contain useful images. Furthermore orthogonal statistical modes describing time variations are present in the rows of $\mathbf{V}^{\mathrm{T}}$ known as principal components (PCs). The PCs cannot be displayed as an image but have been proposed to allow defect depth estimation. This requires isolating the defective region and performing SVD separately on each identified defect. Not much work has been performed to show the accuracy of this estimation which is also an inversion method requiring knowledge of thermal diffusivity.

The matrix $\mathbf{U}$ can be rearranged as a three-dimensional matrix to produce a sequence of EOF images. Figure 2.8 illustrates the first four orthogonal statistical modes. The first EOF does not show much variability. However the second and third EOFs describe the most characteristic variability in the thermal data such as defects, vignetting effects and cooling near the sample boundaries. The third EOF remarkably shows the surface wrinkles of the composite plies near the top left corner. The forth EOF shows the introduction of noise and possible heating effects.

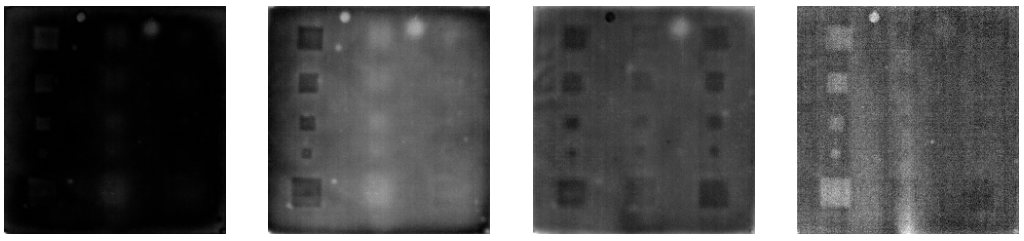

(a) EOF 1 (b) EOF 2 (c) EOF 3 (d) EOF 4

Figure 2.8: Empirical orthogonal functions describing the most variability in the thermal sequence for GFRP106A

2.8 Thermal Signal Reconstruction (TSR)

Thermal signal reconstruction fits a nth order polynomial to a logarithmic sequence of the individual pixel's thermal response. The thermal response can be linearised by transforming to a logarithmic domain before performing a least squares fit (Balageas & Roche, 2014):

$$\ln(\Delta T_{surf}(t)) = \sum_{i=0}^{n} a_i (\ln(t))^i \ . \tag{2.8.1}$$

By using the semi-infinite solution to characterise the step-heating thermal response, the logarithmic domain can be seen to be valuable in linearising the data regardless of thermal properties. The logarithm transform of the semi-infinite solution is

$$\ln(\Delta T_{surf}(t)) = \ln\left(\frac{2Q}{e}\right) + \frac{1}{2}\ln\left(\frac{t}{\pi}\right) \tag{2.8.2}$$

where the response will follow a positive $\frac{1}{2}$ slope and $\frac{2Q}{e}$ describes a constant offset. Because the real temperature response does not practically follow the the semi-infinite response, the choice of order n should be small to avoid unwanted oscillations in the fit but should be large enough to capture the curvature of the data. The data can be reconstructed by taking the exponential of Equation 2.8.1. The reconstructed signal improves defect sensitivity by reducing blurring and increasing signal-to-noise ratio.

Representing the thermal response as a polynomial provides an additional feature of being able to calculate the first and second derivatives. Taking the derivatives of the raw signal is problematic when the signal possesses a high noise content. The derivatives provide an autonomous way of facilitating detection of early time of maximum contrast. The first and second derivatives of the pixel's thermal history in the logarithmic domain is respectively expressed as (Shepard et al., 2003)

$$\frac{d\ln(\Delta T_{surf}(t))}{d\ln(t)} = \sum_{n=0}^{N} n a_n \ln(t)^{n-1} \tag{2.8.3}$$

$$\frac{d^2\ln(\Delta T_{surf}(t))}{d\ln(t)^2} = \sum_{n=0}^{N} n(n-1) a_n \ln(t)^{n-2} \tag{2.8.4}$$

where the resulting logarithmic time derivatives are transformed back into linear time domain by the taking the exponential. The derivatives have proven to provide higher defect contrasts and are valuable in depth estimation in pulsed thermography.

2.9 Summary of Algorithms

The processing methods described here have been selected as the best suited for trasient thermographic data. Other processing methods like filtered thermal contrast (Grys & Minkina, 2010) and partial least squares regression (López et al., 2014(a) & 2014(b))will be added in the future. Many of the methods can be simply applied while others require a level of user interaction. The typical procedures for thermographic data can be first performed with preprocessing methods as suggested in Figure 2.9. These preprocessing methods include subtraction of a pre-flash image to remove partial inhomogeneities already present in the cold images, noise reduction through 3×3 adaptive median and Gaussian low pass filter or application of a smoothing procedure, such as thermal signal reconstruction or polynomial fitting. The fitting speeds up the subsequent processing methods, even though the fitting method can be computationally expensive at first. Normalization and histogram adjustment have proven to be simple procedures of adjusting the visual threshold.

Choosing a processing method will depend on the thermal data itself and will require trial and error inspections of the processed image. The main goal of these methods are to enhance the overall contrast of defects, especially when the image is contaminated by reflections and non-homogeneous surface effects. Contrast methods are generally used after some preprocessing is performed so a better signal can be achieved. These methods are mainly considered for depth inversion methods where depth is a function of contrast. The derivatives, Fourier transform and wavelet transform offer an alternative depth inversion techniques.

After the image is processed the image can be further enhanced by either multiscale retinex or histogram equalization and followed by pseudocolours and contrast methods. The pseudocolours provide a better description of small variabilities.

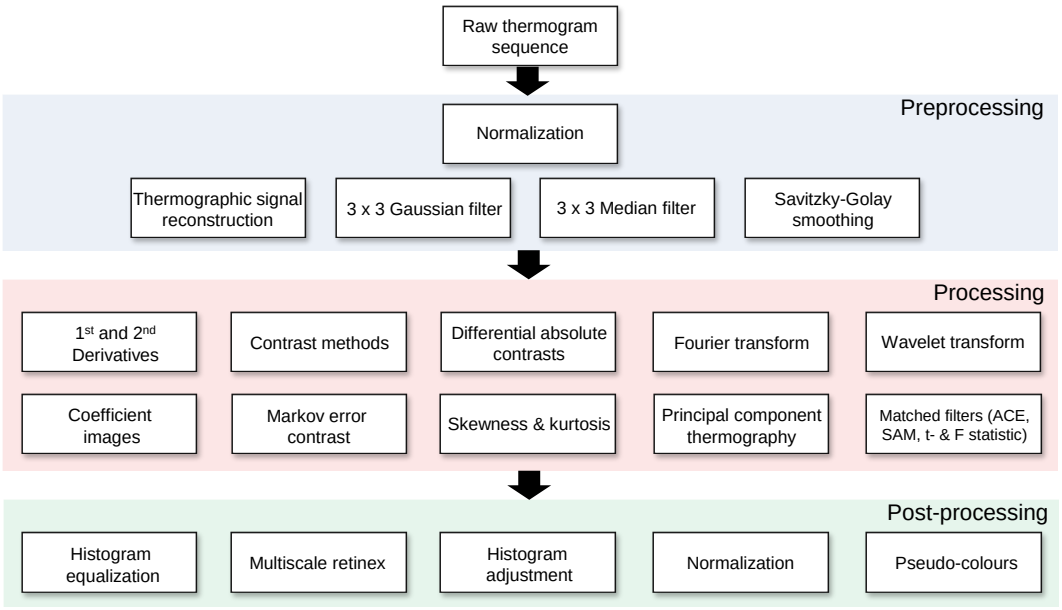

Figure 2.9: The application of signal processing methods at different processing stages

References

Abate, J & Whitt, W, 2006. “A Unified Framework for Numerically Inverting Laplace Transforms”, Informs Journal of Computing, Vol.18, No.4, pp.408-421.

Abdullah-Al-Wadud, M, Hasanul Kabir, M,D, Ali Akber Dewan, M, & Chae, O, 2007. ”A Dynamic Histogram Equalization for Image Contrast Enhancement”, IEEE Trans., Consumer Electronics, Vol.53, No.2, pp.593-600.

Balageas, D.L, Delpech, Ph, Boscher, D & Déom, A, 1991. “New Developments in Stimulated Infrared Thermography Applied to Nondestructive Testing of Laminates”, Rev. of Progress in QNDE 10A, pp.1073-1081.

Balageas, D.L, 2012. “Defense and Illustration of Time-resolved Pulsed Thermography for NDE”, Quantitative InfraRed Thermography, Vol.9, No.1, pp.3-32.

Balageas D & Roche J.M, 2014. “Common Tools for Quantitative Time-resolved Pulse and Step Heating Thermography, Part I: Theoretical Basis”, Quantitative InfraRed Thermography Journal.

Benítez, H, Maldague, X, Ibarra-Castanedo, C, Loaiza, H, Bendada, A & Caicedo, E, 2006. “Modified Differential Absolute Contrast Using Thermal Quadrupoles for the Nondestructive Testing of Finite Thickness Specimens by Infrared Thermography”, in Electrical and Computer Engineering, CCECE, pp.1039-1042.

Borokov, A.A, 1999. “Mathematical Statistics”, Taylor & Francis.

Foy, B, 2009. “Overview of Target Detection Algorithms for Hyperspectral Data”, Los Alamos

Galmiche, F & Maldague, X, 2000. “Depth Defect Retrieval Using the Wavelet Pulsed Phased Thermography”, In Proc. Eurotherm Seminar, No.64, pp.194-199.

González, D, Ibarra-Castanedo, C, Pilla, M, Klein, M & Maldague, X, 2004a. "Automated Differential Absolute Contrast", Quantitative Infrared Thermography.

Gonzalez, R.C, Woods, R.E & Eddins, S.L, 2004. "Digital Image Processing Using MATLAB", Prentice-Hall, Revision: 1.5.

Ibarra-Castanedo, C, 2005. "Quantitative Subsurface Defect Evaluation by Pulsed Phase Thermography:Depth Retrieval with the Phase". Ph. D. Thesis, Laval University, Quebec.

Jobson, D.J, Rahman, Z & Woodell, G.A, 1997. "A Multiscale Retenix for Bridging the Gap Between Colour Images and the Human Observation of Scenes", IEEE Transactions on Image Processing, Vol.6, No.7, pp.965-976.

Klein, M, Ibarra-Castanedo, C, Bendada, A.H & Maldague, X, 2008a. "Thermographic Signal Processing Through Correlation Operators in Pulsed Thermography", in Thermosense XXX, SPIE Defense and Security Symposium, Vavilov, V.P & Burleigh, D.D (Eds.), Vol.6939, pp.693-915, Orlando, Florida, USA.

Madruga, F.J, Ibarra-Castanedo, C, Conde, O.M, López-Higuera, J.M & Maldague, X, 2008. "Automatic Data Processing Based on the Skewness Statistic Parameter for Subsurface Defect Detection by Active Infrared Thermography", 9th International Conference on Quantitative InfraRed Thermography, Krakow, Poland.

Madruga, F.J, Ibarra-Castanedo, C, Conde, O.M, Maldague, X.P & López-Higuera, J.M, 2009. "Enhanced Contrast Detection of Subsurface Defects by Pulsed Infrared Thermography Based on the Fourth Order Statistic Moment, Kurtosis", In SPIE Defense, Security, and Sensing, International Society for Optics and Photonics, pp.72990U-72990U.

Maillet, D, André, S, Batsale, J, Degiovanni, A & Moyne, C, 2000. "Thermal Quadrupoles: Solving the Heat Equation Through Integral Transforms", John Wiley and Sons, USA.

Maldague, X.P, 2001. "Theory and Practice of Infrared Technology for Nondestructive Testing", Hoboken: John Wiley & Sons, Inc.

Maldague, X, Galmiche, F & Ziadi, A, 2002. "Advances in Pulsed Phase Thermography", Journal of Infrared Physics & Technology, Vol.43, pp.175-181.

Larsen, C.A, 2011. "Document flash thermography", All Graduate Theses and Dissertations. Paper 1018.

Park, G.H, Cho, H.H & Choi, M.R, 2008. "A Contrast Enhancement Method Using Dynamic Range Separate Histogram Equalization", IEEE Transactions on Consumer Electronics, Vol.54, pp.1981-1987.

Rahman, Z, Woodell, G.A & Jobson, D.J, 2001. "Retinex Image Enhancement: Application to Medical Images", Presented at the NASA workshop on New Partnerships in Medical Diagnostic Imaging, Greenbelt, Maryland.

Shannon, C.E, 1949. "Communication in presence of noise", Proc. IRE, Vol.37, pp.10-21.

Sheet, D, Garud, H, Suveer, A, Mahadevappa, M & Chatterjee, J, 2010. "Brightness Preserving Dynamic Fuzzy Histogram Equalization", in Consumer Electronics, IEEE Transactions, Vol.56, No.4, pp.2475-2480.

Shepard, S, Lahota, J, Rubadeux, B, Wang,D & Ahmed, T, 2003. "Reconstruction and Enhancement of Active Thermography Image Sequences", Optical Engineering, Vol.42, Issue 5, pp.1337-1342.

Štruc, V, Žibert, J & Pavešić, N, 2009. "Histogram Remapping as a Preprocessing Step for Robust Face Recognition", WSEAS Transactions on Information Science and Applications, Vol.6, No.3, pp.520-529.

Usamentiaga,R, Venegas, P, Guerediaga, J, Vega, L & López, I, 2012. "A Quantitative Comparison of Stimulation and Post-Processing Thermographic Inspection Methods Applied to Aeronautical Carbon Fiber Reinforced Polymer",11th International Conference on Quantitative InfraRed Thermography.

Zauner, G, Mayr, G & Hendorfer, G, 2010. "Subsurface Defect Characterization in Pulsed Phase Thermography by Means of Wavelet Analysis", In 2nd International Symposium on NDT in Aerospace, Tu, Vol.1.